Supplement of Geosci. Model Dev., 15, 4239–4258, 2022
https://doi.org/10.5194/gmd-15-4239-2022-supplement

Geoscientific Model Development
Open Access

Supplement of

Assessing the roles emission sources and atmospheric processes play in simulating δ^{15}N of atmospheric NO_x and NO_3^- using CMAQ (version 5.2.1) and SMOKE (version 4.6)

Huan Fang and Greg Michalski

Correspondence to: Huan Fang (fang63@purdue.edu)

1. The details of Incorporating ^{15}N into NO_x emission datasets

1.1 Biogenic $^{15}NO_x$ emissions

Biogenic sources of NO_x are predominately by-products of microbial nitrification and denitrification occurring in soil. The Biogenic Emissions Inventory System (BEIS) was implemented within SMOKE to estimate hourly emissions from biogenic sources. The normalized emission was first generated based on 230 land-use types from the Biogenic Emission Landcover Database (USEPA, 2018), a normalized emission factor of NO_x, and land cover, to indicate the emission under standard environmental conditions (at 30 °C and 1000 μmol m^{-2} s^{-1} photosynthetic active radiation). Then, meteorological data generated by MM5 (Fifth-Generation Penn State/NCAR Mesoscale Model) (Grell, Dudhia, & Stauffer, 1994) was incorporated into BEIS and was used to finalize the speciated and temporally allocated emissions from biogenic sources by the algorithm for NO_x. This algorithm uses three steps. First, the land surface was designated by the land use as agriculture and non-agriculture based on Biogenic Emission Landcover Database. Second, NO_x emissions were normalized based on temperature, precipitation, fertilizer application, and crop canopy coverage during the crop growing season (April 1 to October 31). Finally, for NO_x emissions over agriculture areas during the non-growing season and NO_x emissions over non-agriculture areas throughout the year, the emission NO_x factor was limited to that for grassland, and the only temperature was used to normalize NO_x emission (Pierce, 2001; Vukovich & Pierce, 2002; Schwede et al., 2005; Pouliot & Pierce, 2009; USEPA, 2018).

1.2 Mobile $^{15}NO_x$ emissions

The emission of NO_x based on on-road vehicle activity was estimated using MOBILE6, a model developed by the EPA's Office of Transportation and Air Quality. There are three main factors that are considered to estimate on-road vehicle NO_x emissions. The first is the emission rate per mile traveled for 28 different classifications of vehicles. The second is the emission factor based on 10 different types of operating conditions (running, start, hot soak, diurnal, resting, run loss, crankcase, refueling, brake wear, and tire wear), travel speed over 33 different road types with distinct average speed, types of fuel being consumed, and ambient temperature. Finally, the number of vehicles in each classification, emission type, and fuel type along with each type of roadway during certain periods (USEPA, 2003; Houyoux, 2005). MOBILE6 and SMOKE were used to determine NO_x emissions along the roadways and were converted into hourly emissions within each 12 km × 12 km grid cell.

1.3 Area source $^{15}NO_x$ emissions

Area sources are the stationary anthropogenic NO_x emissions that spread over a spatial extent and are individually too small in magnitude to report as point sources. These include NO_x emitted by off-road vehicles, residential combustion (anthracite coal, bituminous coal, distillate oil, residual oil, natural gas, liquified petroleum gas, and wood), industrial processes (chemical manufacturing, food, and kindred products, metal production, mineral processes, petroleum refining, wood products, construction, machinery, mining, and quarrying, etc), agriculture production (crops, fertilizer application, livestock, animal waste, etc), solvent utilization, storage and transport, waste disposal, treatment, and recovery, forest wildfires, as well as road dust and fugitive dust. Among these, livestock and off-road vehicles are dominant, accounting for nearly 90% of area NO_x emissions across the contiguous United States (Houyoux, 2005). The annual area emissions from the NEI sectors were estimated at the county level and evenly divided into hourly emissions over the 12 km × 12 km grid for use in chemical transport modeling.

SMOKE Processing Category	Emission Source
Biogenic	By-products of microbial nitrification and denitrification occurring in soil
Area	Off-road vehicles Residential combustion: *anthracite coal, bituminous coal, distillate oil, residual oil, natural gas, liquified petroleum gas, and wood* Industrial processes: *chemical manufacturing, food, and kindred products, metal production, mineral processes, petroleum refining, wood products, construction, machinery, mining, and quarrying, etc.* Agriculture production: *crops, fertilizer application, livestock, animal waste, etc.* Solvent utilization Storage and transport Waste disposal, treatment, and recovery Forest wildfires Road dust and fugitive dust
Mobile	On-road vehicles
Point	Electric generating units (EGU) Commercial combustion and industrial combustion (non-EGU) Fugitive dust

Table S1: Categorization of emission sources

2. The details of MCIP simulation

The MCIP first obtains the necessary parameters (Table S2) from WRF outputs. Then the MCIP extracts the data of the necessary parameters for the appropriate geographic domain, which are slightly smaller than the domain of WRF outputs since the cells near the boundary are inadequate for CMAQ simulation. For example, the geographic domain of WRF outputs for this research is 160 grids in the east-west direction and 151 grids in the north-south direction. Therefore, MCIP extracts the WRF outputs into 157 grids in the east-west direction and 148 grins in the north-south direction, which are exactly the same as the emission input dataset prepared from section 2.1 and are adequate for CMAQ simulation. After that, MCIP converts the units of the parameters into the units, which are consistent with the CMAQ simulation. For example, the 10-meter wind is displayed as u (east-west) and v (north-south) component of wind vector in WRF but is displayed as wind speed and wind direction in CMAQ. If the parameters, which are necessary for running CMAQ, are not available from the WRF output, MCIP will diagnose and compute them, such as PBL (planetary boundary layer) parameters and cloud information (cloud top, cloud base, liquid water content, cloud coverage). The MCIP also conducts the interpolation and mass-weighted averaging of data, if the grid resolutions of WRF and CMAQ are different. Finally, MCIP organizes the parameters into seven netCDF files that embedded with I/O API (input/output applications programming interface): 2-D time-independent fields at cell centers, 2-D time-independent fields on domain perimeter, 2-D time-independent fields at cell corners, 2-D time-dependent fields at cell centers, 3-D time-dependent fields at cell centers, 3-D time-dependent fields on domain perimeter, and 3-D time-dependent fields at cell corners (Table S3).

Variable Name	Description	Unit	File
LAT	latitude (cell centers)	degree	GRIDBDY2D, GRIDCRO2D
LON	longitude (cell centers)	degree	GRIDBDY2D, GRIDCRO2D
MSFX2	squared map-scale factor (cell centers)	m^2 m^{-2}	GRIDBDY2D, GRIDCRO2D
HT	terrain elevation	m	GRIDBDY2D, GRIDCRO2D
DLUSE	dominant land use	category	GRIDBDY2D, GRIDCRO2D
LWMASK	land-water mask	category	GRIDBDY2D, GRIDCRO2D
PURB	urban percent of cell based on land coverage	percent	GRIDBDY2D, GRIDCRO2D
LUFRAC	fraction of land use by category	unitless	GRIDBDY2D, GRIDCRO2D
LATD	latitude (cell corners)	degree	GRIDDOT2D
LOND	longitude (cell corners)	degree	GRIDDOT2D
MSFD2	squared map scale factor (cell corners)	m^2 m^{-2}	GRIDDOT2D
LATU	latitude (cell west-east faces)	degree	GRIDDOT2D
LONU	longitude (cell west-east faces)	degree	GRIDDOT2D
MSFU2	squared map scale factor (cell west-east faces)	m^2 m^{-2}	GRIDDOT2D
LATV	latitude (cell south-north faces)	degree	GRIDDOT2D
LONV	longitude (cell south-north faces)	degree	GRIDDOT2D
MSFV2	squared map scale factor (cell south-north faces)	m^2 m^{-2}	GRIDDOT2D
JACOBF	total Jacobian (layer face)	m	METBDY3D, METCRO3D
JACOBM	total Jacobian (layer middle)	m	METBDY3D, METCRO3D
DENSA_J	Jacobian-weighted total air density	kg m^{-2}	METBDY3D, METCRO3D

WHAT_JD	Jacobian- and density-weighted vertical contravariant velocity	kg m^{-1} s^{-1}	METBDY3D, METCRO3D
TA	air temperature	K	METBDY3D, METCRO3D
QV	water vapor mixing ratio	kg kg^{-1}	METBDY3D, METCRO3D
PRES	air pressure	Pa	METBDY3D, METCRO3D
DENS	air density	kg m^{-3}	METBDY3D, METCRO3D
ZH	mid-layer height above ground	m	METBDY3D, METCRO3D
ZF	full layer height above ground	m	METBDY3D, METCRO3D
QC	cloud water mixing ratio	kg kg^{-1}	METBDY3D, METCRO3D
QR	rain water mixing ratio	kg kg^{-1}	METBDY3D, METCRO3D
CFRAC_3D	3D resolved cloud fraction	unitless	METBDY3D, METCRO3D
PRSFC	surface pressure	Pa	METCRO2D
USTAR	cell-averaged horizontal friction velocity	m s^{-1}	METCRO2D
WSTAR	convective velocity scale	m s^{-1}	METCRO2D
PBL	planetary boundary layer height	m	METCRO2D
ZRUF	surface roughness length	m	METCRO2D
MOLI	inverse Monin-Obukhov length	m^{-1}	METCRO2D
HFX	sensible heat flux	W m^{-2}	METCRO2D
LH	latent heat flux	W m^{-2}	METCRO2D
RADYNI	inverse aerodynamic resistance	m s^{-1}	METCRO2D
RSTOMI	inverse bulk stomatal resistance	m s^{-1}	METCRO2D
TEMPG	skin temperature at ground	K	METCRO2D
TEMP2	2-m temperature	K	METCRO2D
Q2	2-m water vapor mixing ratio	m s^{-1}	METCRO2D

WSPD10	10-m wind speed	m s^{-1}	METCRO2D
WDIR10	10-m wind direction	degree	METCRO2D
GLW	longwave radiation at ground	W m^{-2}	METCRO2D
RGRND	solar radiation absorbed at ground	W m^{-2}	METCRO2D
RN	non-convective precipitation over interval	cm	METCRO2D
RC	convective precipitation over interval	cm	METCRO2D
CFRAC	total column integrated cloud fraction	unitless	METCRO2D
CLDT	cloud layer top height	m	METCRO2D
CLDB	cloud layer bottom height	m	METCRO2D
WBAR	average liquid water content of cloud	g m^{-3}	METCRO2D
SNOCOV	snow cover	category	METCRO2D
VEG	vegetation coverage	unitless	METCRO2D
LAI	leaf-area index	m^2 m^{-2}	METCRO2D
SEAICE	sea ice	unitless	METCRO2D
WR	canopy moisture content	m	METCRO2D
SOIM1	volumetric soil moisture in near-surface soil	m^3 m^{-3}	METCRO2D
SOIM2	volumetric soil moisture in deep soil	m^3 m^{-3}	METCRO2D
SOIT1	soil temperature in near-surface soil	K	METCRO2D
SOIT2	soil temperature in deep soil	K	METCRO2D
SLTYP	soil texture type	category	METCRO2D
UWIND	u-component of horizontal wind (cell corners)	m s^{-1}	METDOT3D
VWIND	v-component of horizontal wind (cell corners)	m s^{-1}	METDOT3D
UHAT_JD	contravariant U-component wind×density×Jacobian	kg m^{-1} s^{-1}	METDOT3D
VHAT_JD	contravariant V-component wind×density×Jacobian	kg m^{-1} s^{-1}	METDOT3D
UWINDC	u-component of horizontal wind (west-east cell faces)	m s^{-1}	METDOT3D
VWINDC	v-component of horizontal wind (south-north cell faces)	m s^{-1}	METDOT3D

Table S2: MCIP output variables

File Name	Description	Time-Dependence	Spatial Dimensions
GRIDCRO2D	2-D time-independent fields at cell centers	Independent	X*Y
GRIDBDY2D	2-D time-independent fields on domain perimeter	Independent	Perimeter*Z
GRIDDOT2D	2-D time-independent fields at cell corners	Independent	(X+1)*(Y+1)
METCRO2D	2-D time-dependent fields at cell centers	Hourly	X*Y
METCRO3D	3-D time-dependent fields at cell centers	Hourly	X*Y*Z
METBDY3D	3-D time-dependent fields on domain perimeter	Hourly	Perimeter*Z
METDOT3D	3-D time-dependent fields at cell corners	Hourly	(X+1)*(Y+1)*Z

Table S3: Output files of MCIP

3. Supplementary materials for Results and Discussion

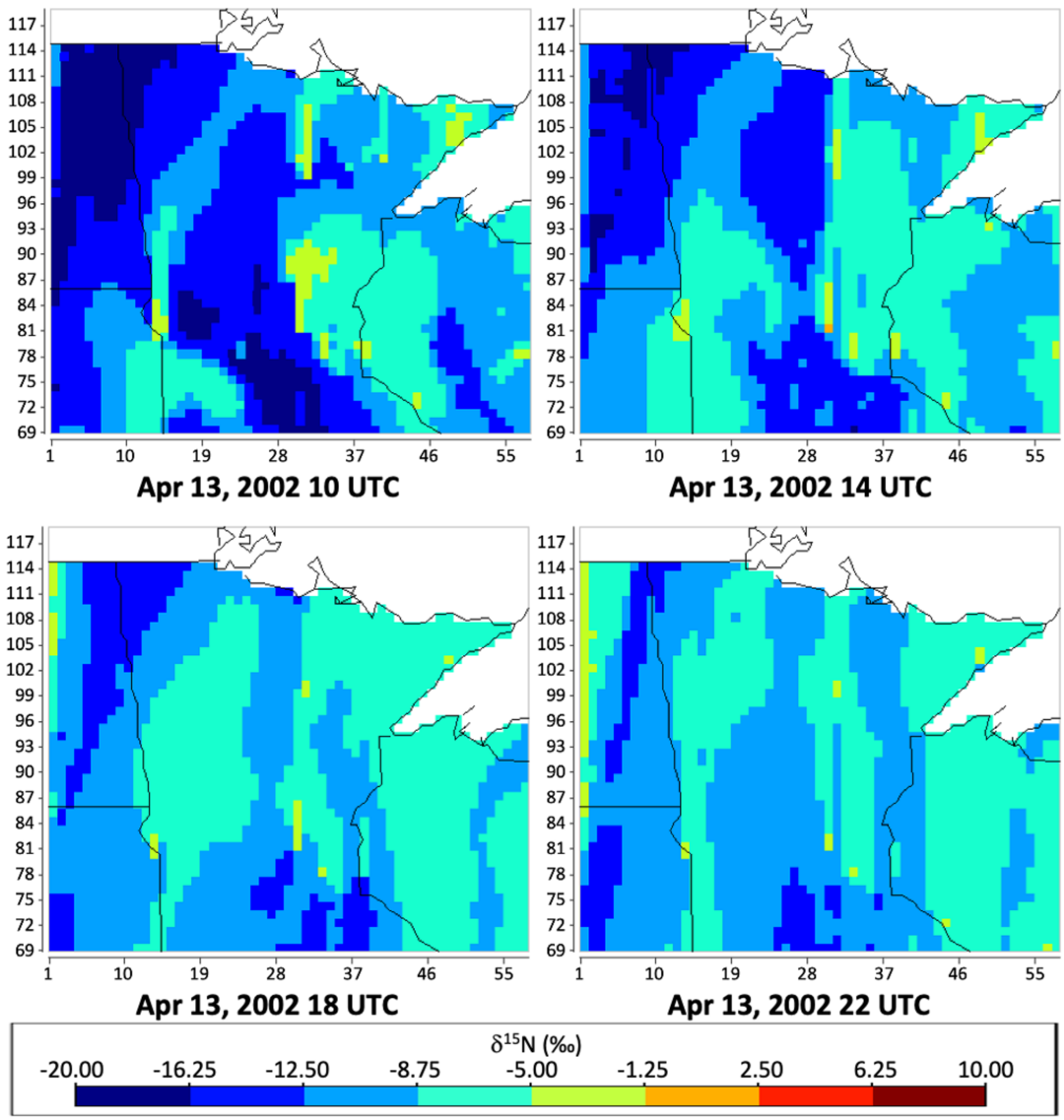

Figure S1: The geographical distribution of the $\delta^{15}N$ value of atmospheric NO_x in per mil (‰) from 10 UTC to 22 UTC on Apr 13, 2002 near the northwest corner of the study domain, simulated by CMAQ, based on NEI-2002 and 2016 meteorology.

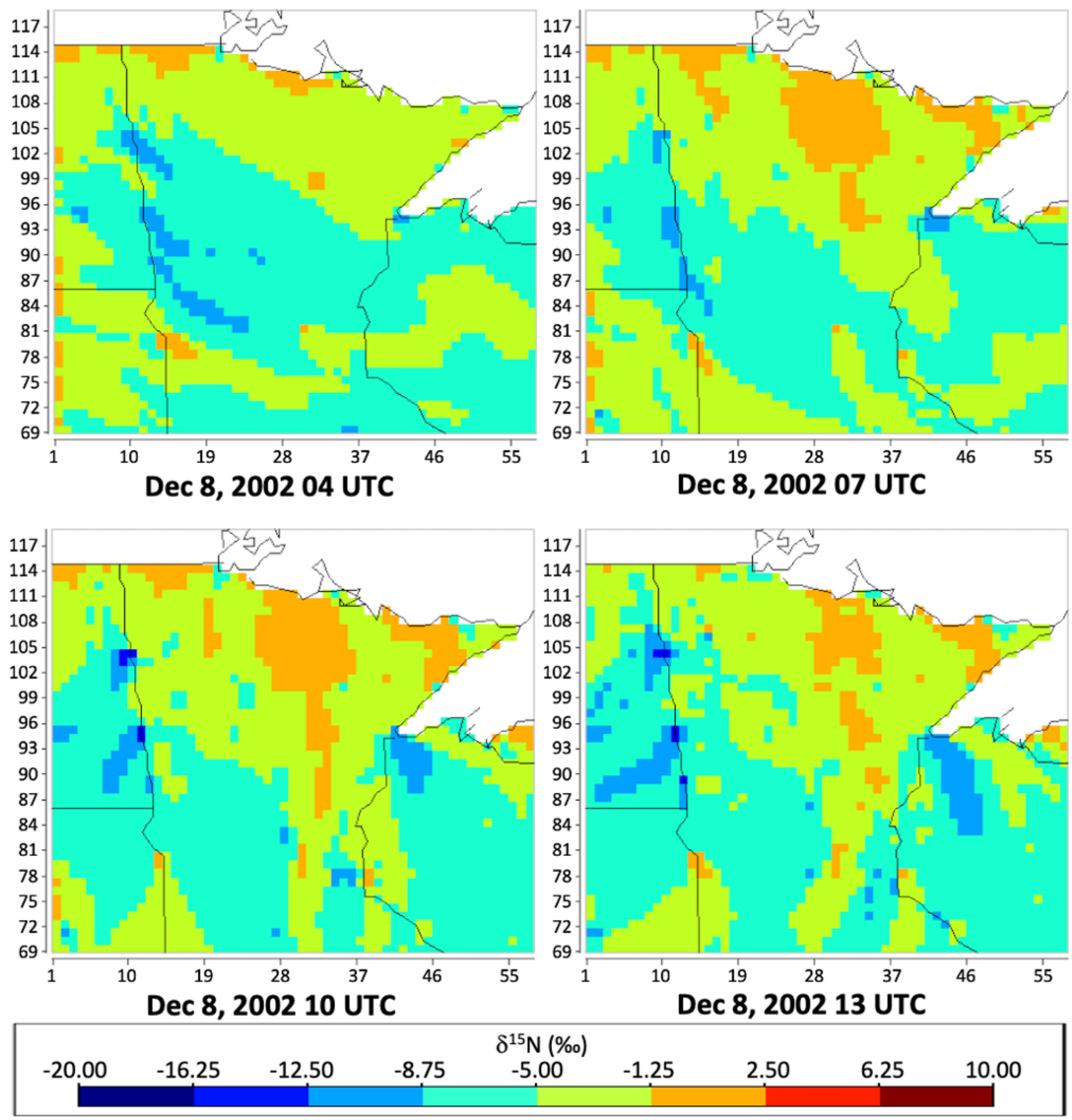

Figure S2: The geographical distribution of the $\delta^{15}N$ value of atmospheric NO_x in per mil (‰) from 04 UTC to 13 UTC on Dec 8, 2002 near the northwest corner of the study domain, simulated by CMAQ, based on NEI-2002 and 2016 meteorology.

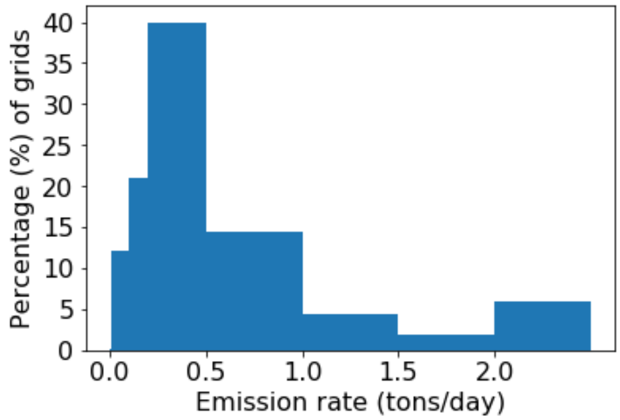

Figure S3: The histogram of total NO_x emission in the Midwest between April and June in tons/day.

Urban Area	SMOKE-simulated emission rate		OMI-derived emission rate
	tons/day	tons/hr	tons/hr
Chicago, IL	634.074	24.42	23.3±9.7
Detroit, MI	288.617	12.026	18.7±7.8
Indianapolis, IN	72.487	3.021	3.1±1.3
Kansas City, MO	150.733	6.281	5.1±2.1
Louisville, KY	61.178	2.549	2.5±1.0
Minneapolis, MN	220.957	9.207	9.3±3.9
St. Louis, MO	99.953	4.165	4.9±2.0

Table S4: The seasonal average NO_x emission rate for major cities in the Midwest

Power Plant Site	SMOKE-simulated emission rate	CEMS-measured emission rate	
	tons/day	kt/yr	tons/day
Paradise, KY	93.414	38.33	105.014
New Madrid, MO	65.777	23.09	63.260
T. Hill Energy Center, MO	38.686	11.95	32.740
Kincaid, IL	38.934	11.92	32.644
Powerton, IL	62.394	21.56	59.068
Jeffrey Energy Center, KS	59.339	21.39	58.603

Table S5: The seasonal average NO_x emission rate for major power plants in the Midwest

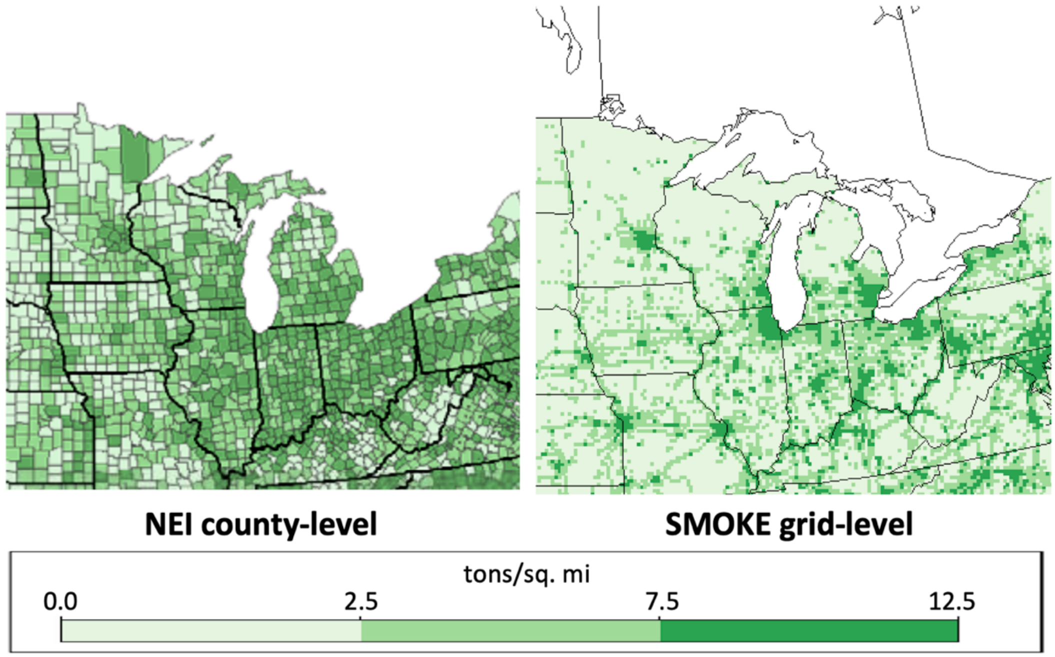

Figure S4: The geographical distribution of 2002 NO_x emission density estimated by NEI over each county (left) and simulated by SMOKE over each grid (right), throughout the Midwest.

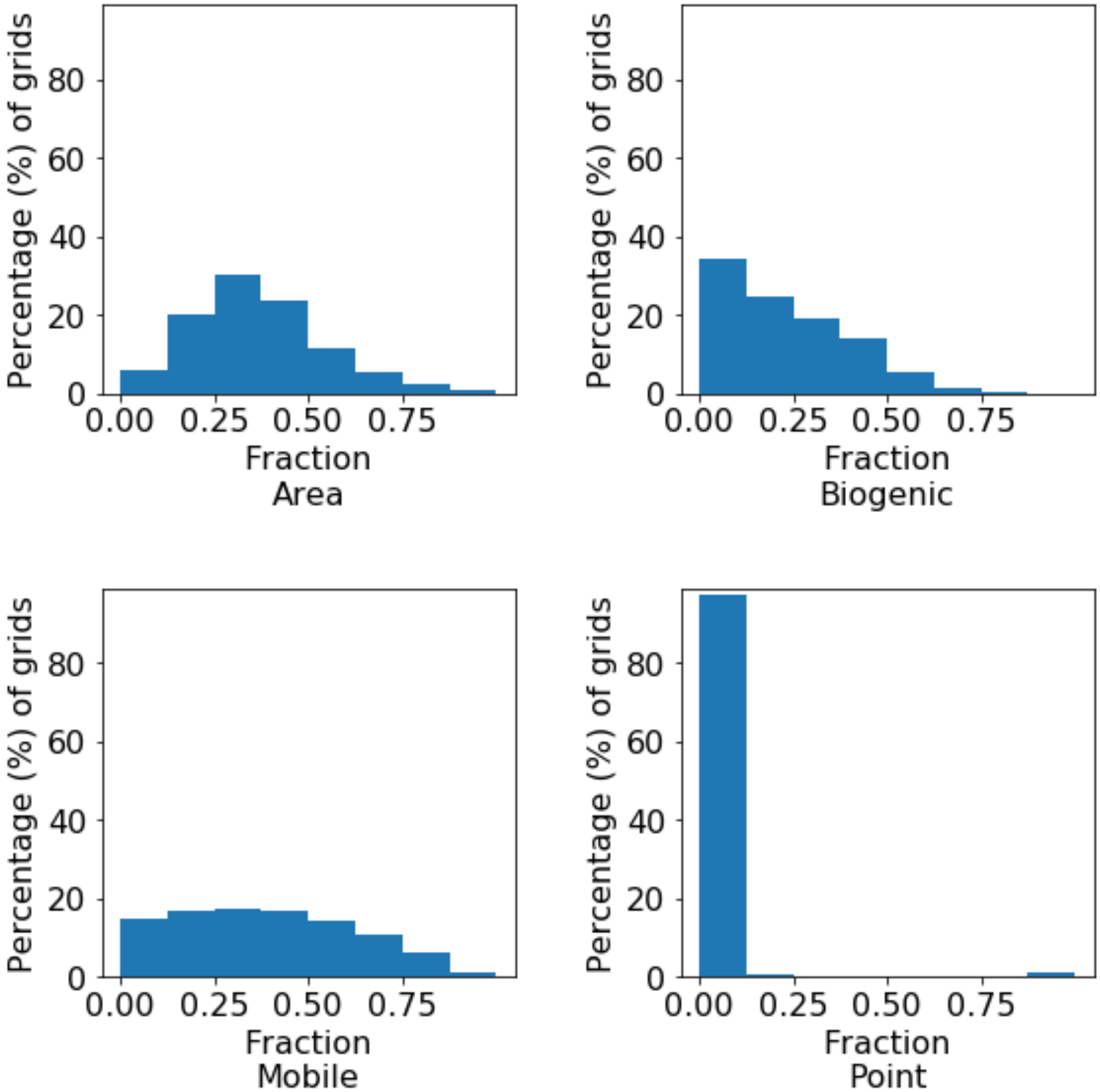

Figure S5: The histogram of the fraction of NO_x emission from each SMOKE processing category (area, biogenic, mobile, point) over each grid throughout the Midwest between April and June based on NEI-2002.

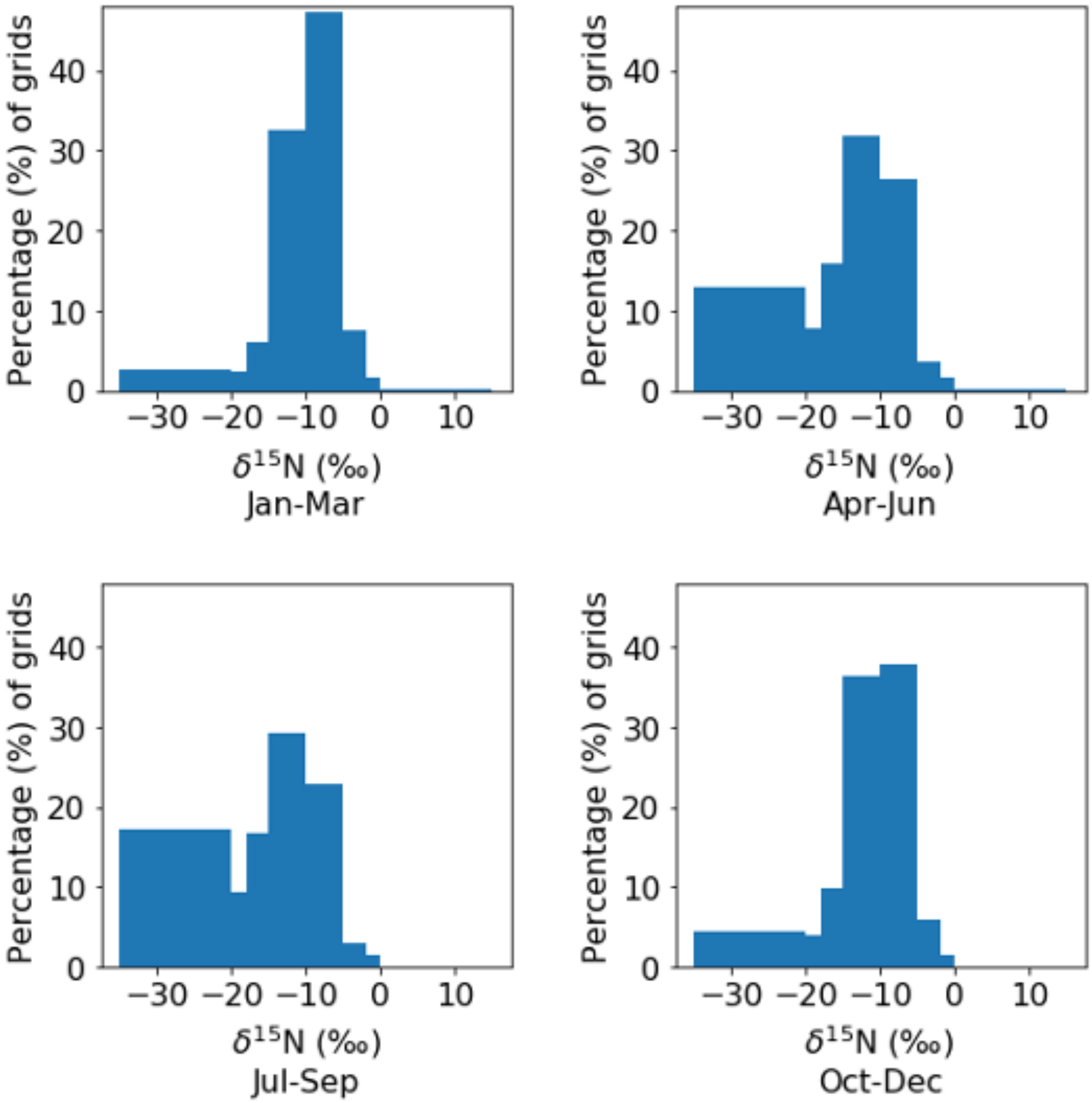

Figure S6: The histogram of the $\delta^{15}N$ of total NO_x emissions in each season (Winter: Jan-Mar; Spring: Apr-Jun; Summer: Jul-Sep; Fall: Oct-Dec) in per mil (‰) over the 12-km grids throughout the Midwest simulated by SMOKE, based on NEI-2002.

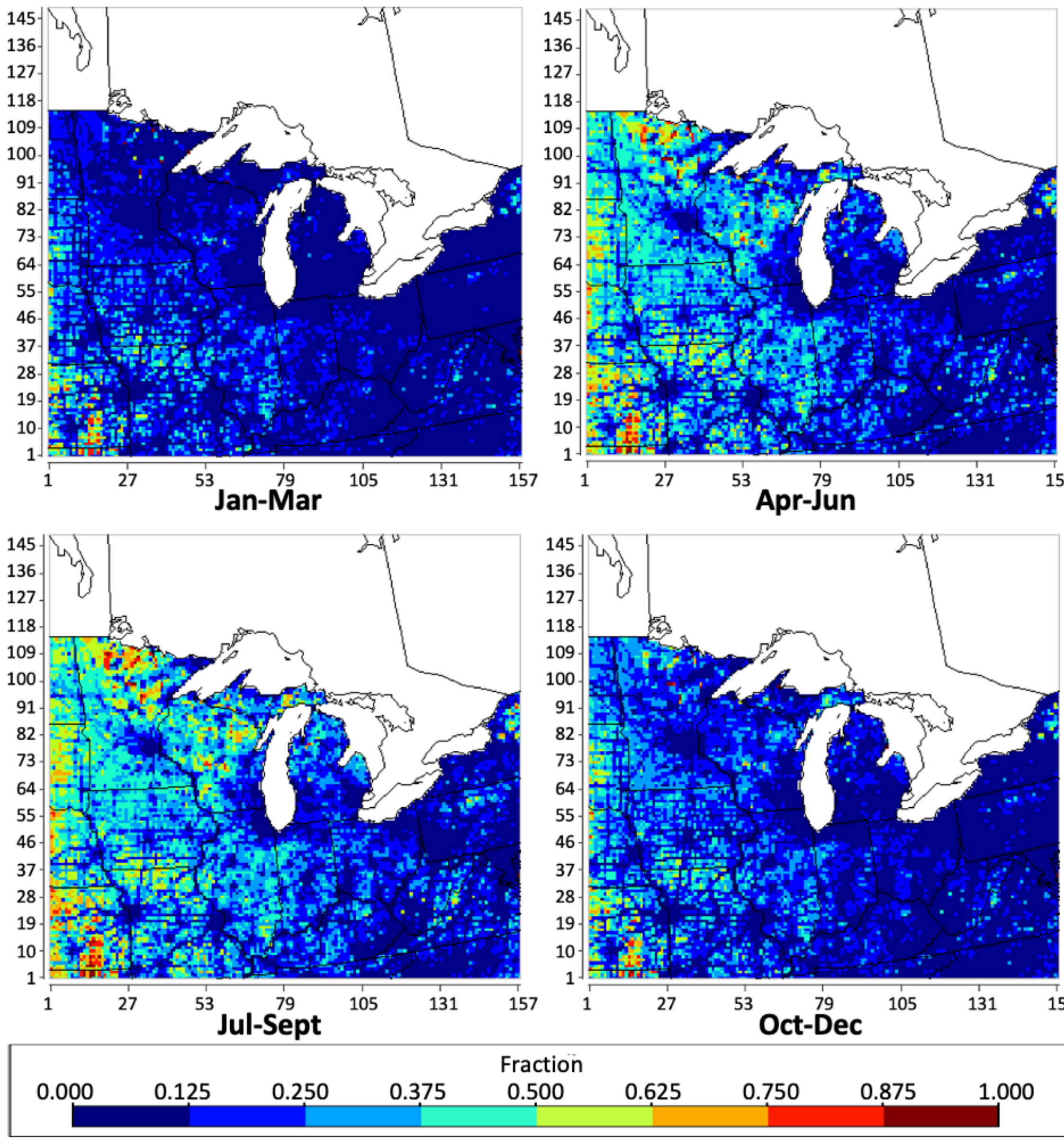

Figure S7: The geographical distribution of the fraction of NO_x emission from biogenic sources over each grid in each season (Winter: Jan-Mar; Spring: Apr-Jun; Summer: Jul-Sep; Fall: Oct-Dec) throughout the Midwest simulated by SMOKE, based on NEI-2002.

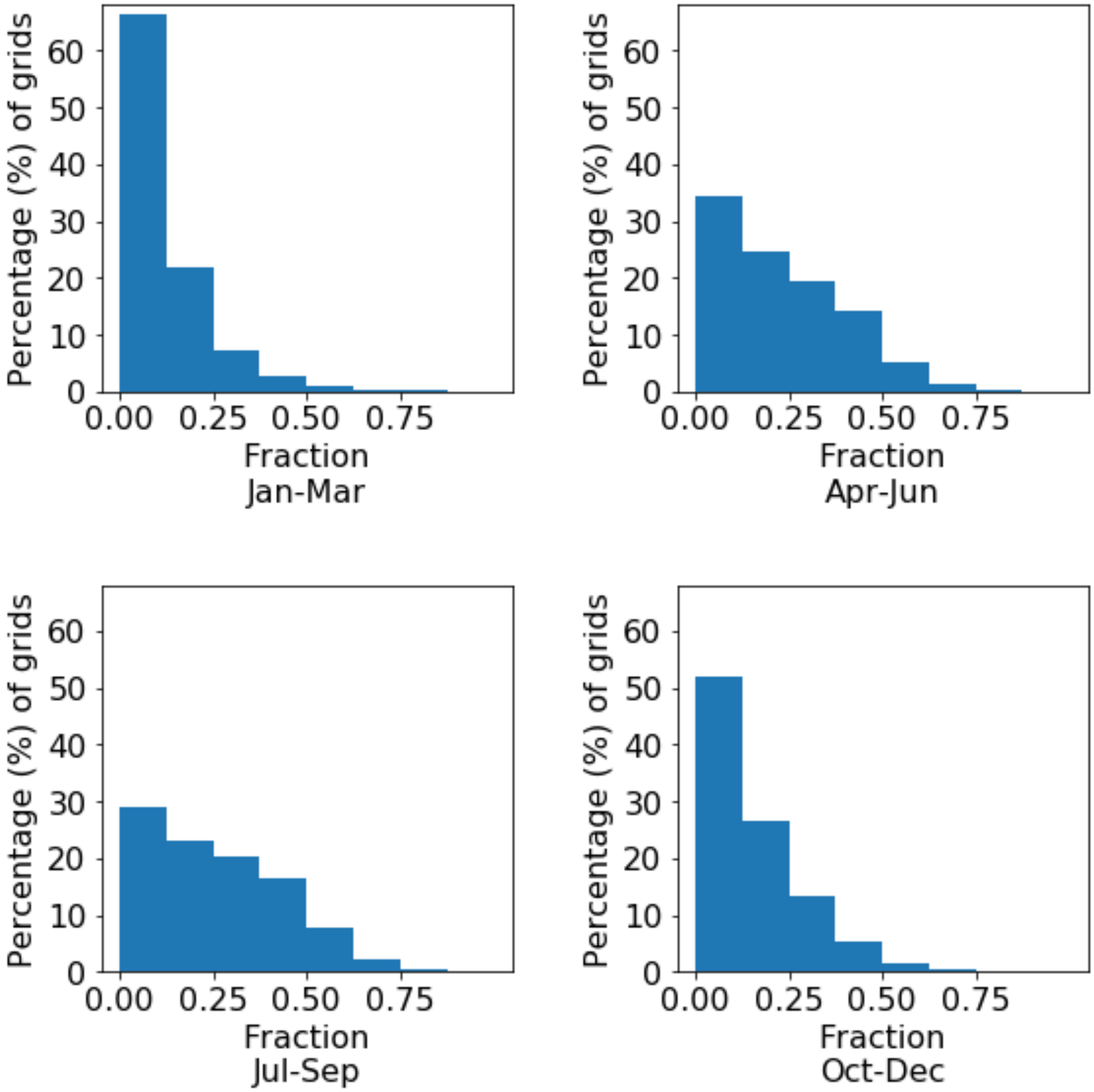

Figure S8: The histogram of the fraction of NO_x emission from biogenic sources over each grid in each season (Winter: Jan-Mar; Spring: Apr-Jun; Summer: Jul-Sep; Fall: Oct-Dec) throughout the Midwest simulated by SMOKE, based on NEI-2002.

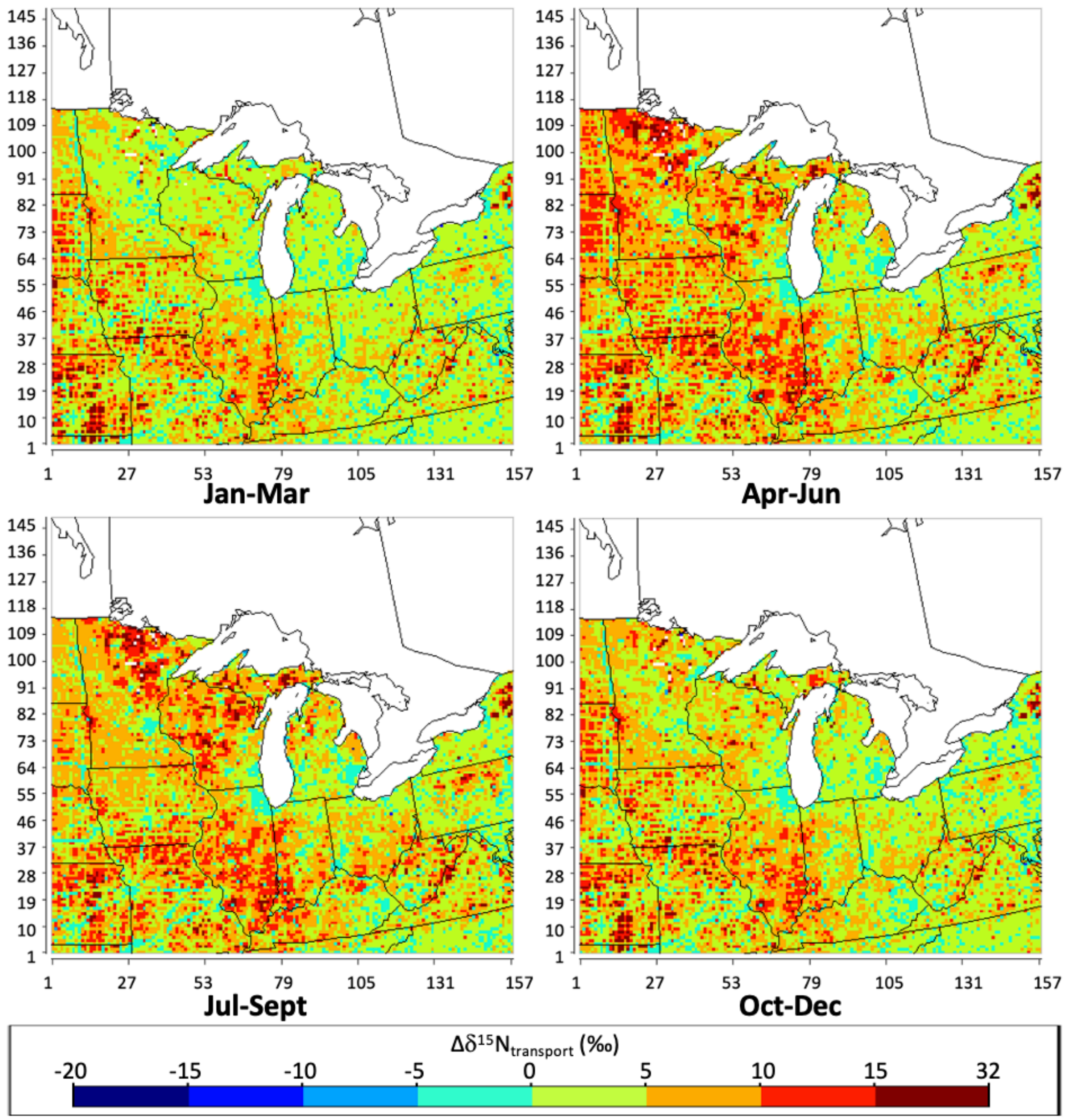

Figure S9: The $\Delta\delta^{15}N_{transport}$ value of atmospheric NO_x ($\delta^{15}N_{emission+transport} - \delta^{15}N_{emission\ only}$) during each season (Winter: Jan-Mar; Spring: Apr-Jun; Summer: Jul-Sep; Fall: Oct-Dec), throughout the Midwest simulated by CMAQ, based on NEI-2002 emissions and 2016 meteorology.

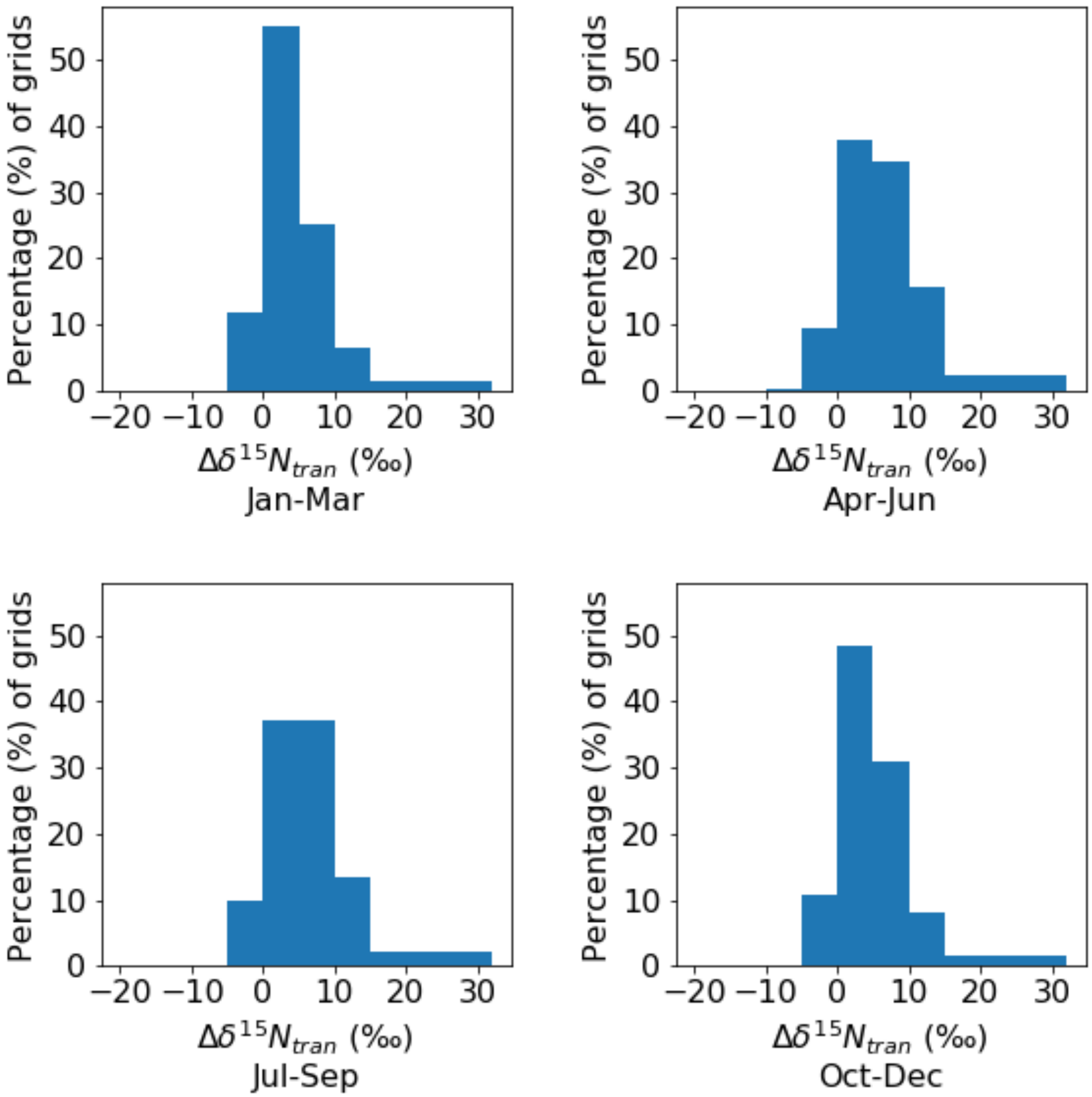

Figure S10: The histogram of the $\Delta\delta^{15}N_{transport}$ value of atmospheric NO_x ($\delta^{15}N_{emission+transport} - \delta^{15}N_{emission\ only}$) during each season (Winter: Jan-Mar; Spring: Apr-Jun; Summer: Jul-Sep; Fall: Oct-Dec), throughout the Midwest simulated by CMAQ, based on NEI-2002 emissions and 2016 meteorology.

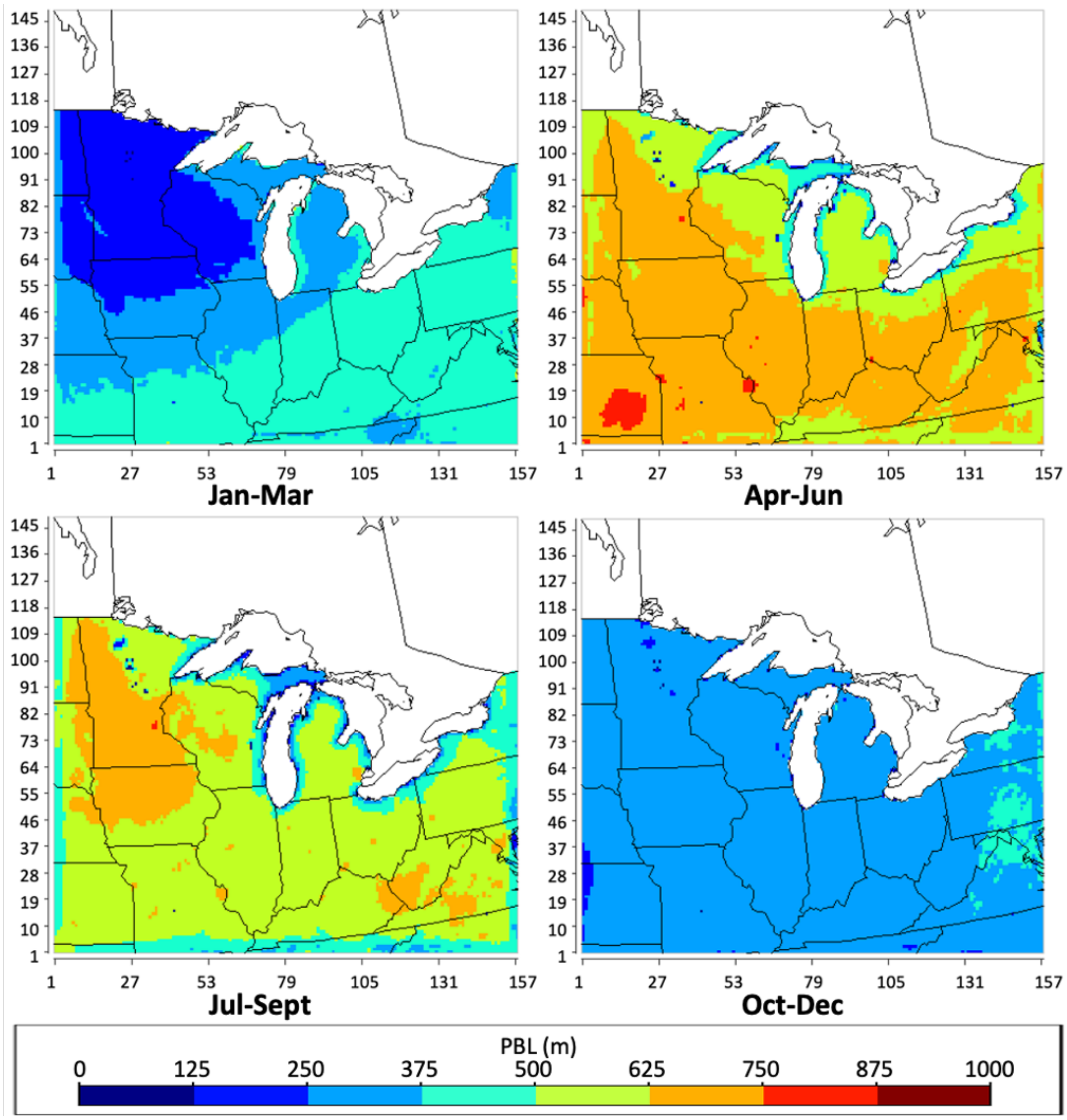

Figure S11: The geographical distribution of the planetary boundary layer (PBL) height in meters during each season (Winter: Jan-Mar; Spring: Apr-Jun; Summer: Jul-Sep; Fall: Oct-Dec) of 2016 throughout the Midwest.

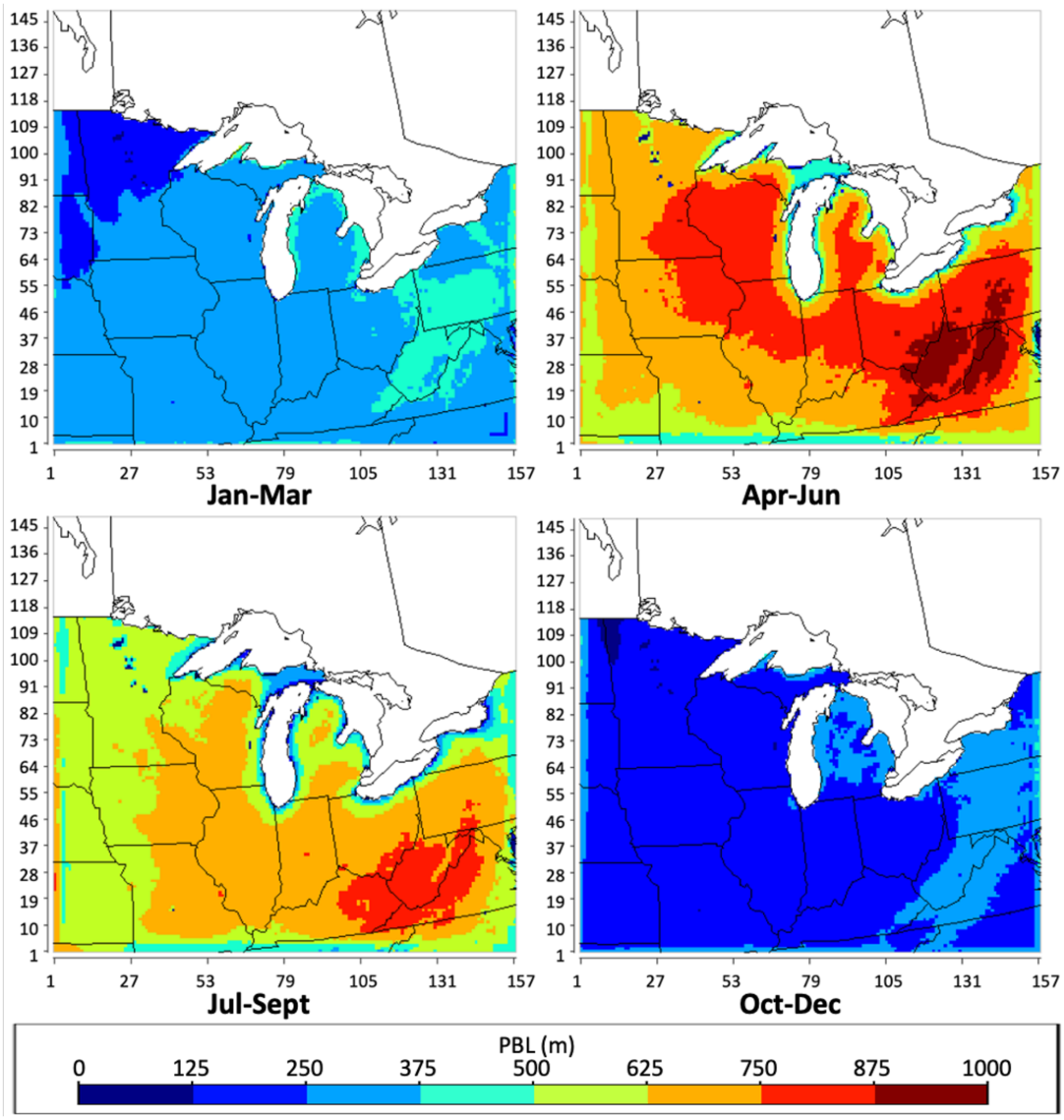

Figure S12: The geographical distribution of the planetary boundary layer (PBL) height in meters during each season (Winter: Jan-Mar; Spring: Apr-Jun; Summer: Jul-Sep; Fall: Oct-Dec) of 2002 throughout the Midwest.

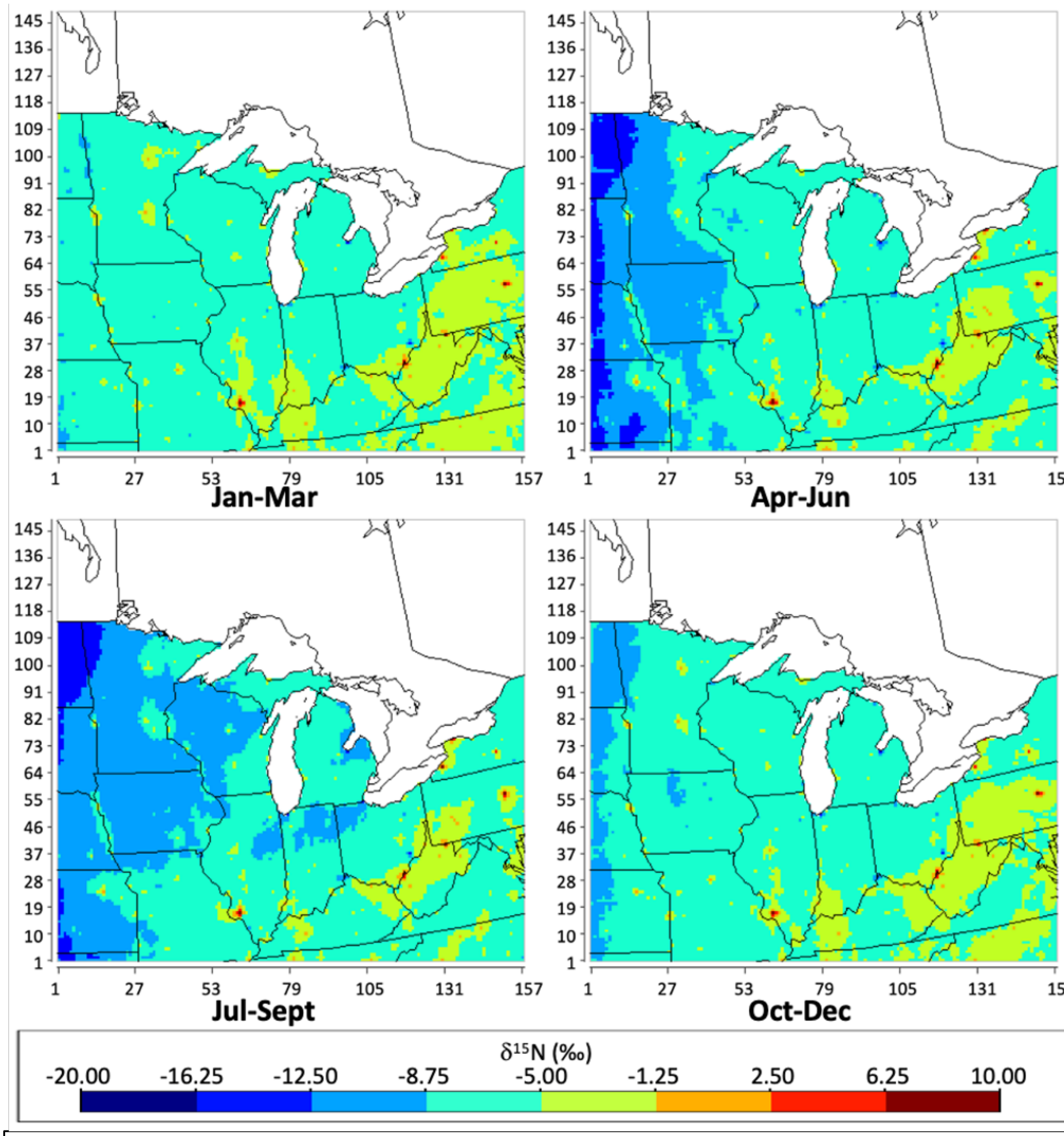

Figure S13: The geographical distribution of the $\delta^{15}N$ value of atmospheric NO_x in each season (Winter: Jan-Mar; Spring: Apr-Jun; Summer: Jul-Sep; Fall: Oct-Dec) in per mil (‰) throughout the Midwest simulated by CMAQ, based on NEI-2002 and 2002 meteorology.

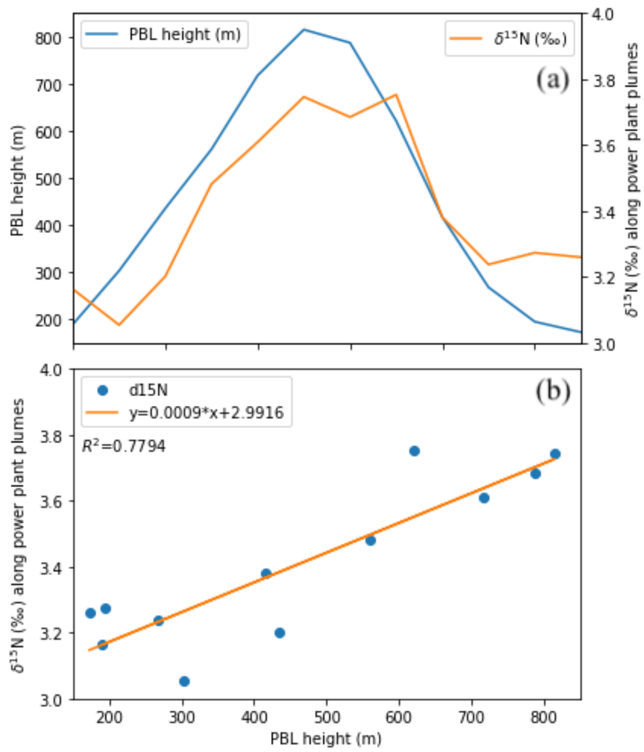

Figure S14: The time series plot (a) and the scatter plot (b) of the domain average PBL height (m) and the average $\delta^{15}N$ (‰) value of atmospheric NO_x along the plumes of power plants during each month throughout the Midwest simulated by CMAQ, based on NEI-2002 and 2002 meteorology.

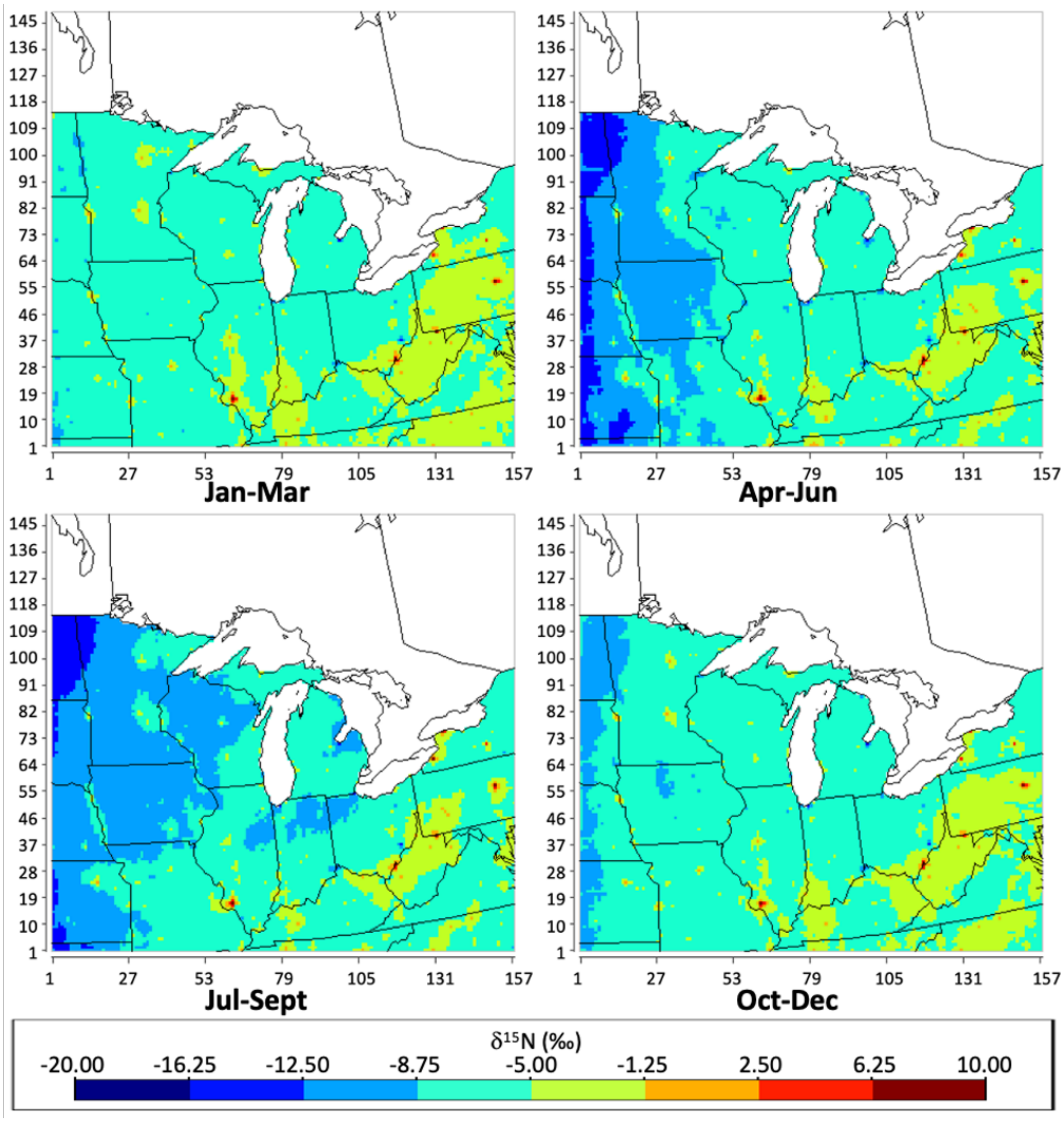

Figure S15: The geographical distribution of the $\delta^{15}N$ value of atmospheric NO_x in each season (Winter: Jan-Mar; Spring: Apr-Jun; Summer: Jul-Sep; Fall: Oct-Dec) in per mil (‰) throughout the Midwest simulated by CMAQ, based on NEI-2002 and 2016 meteorology, under the "enhanced NO_x loss" scenario.

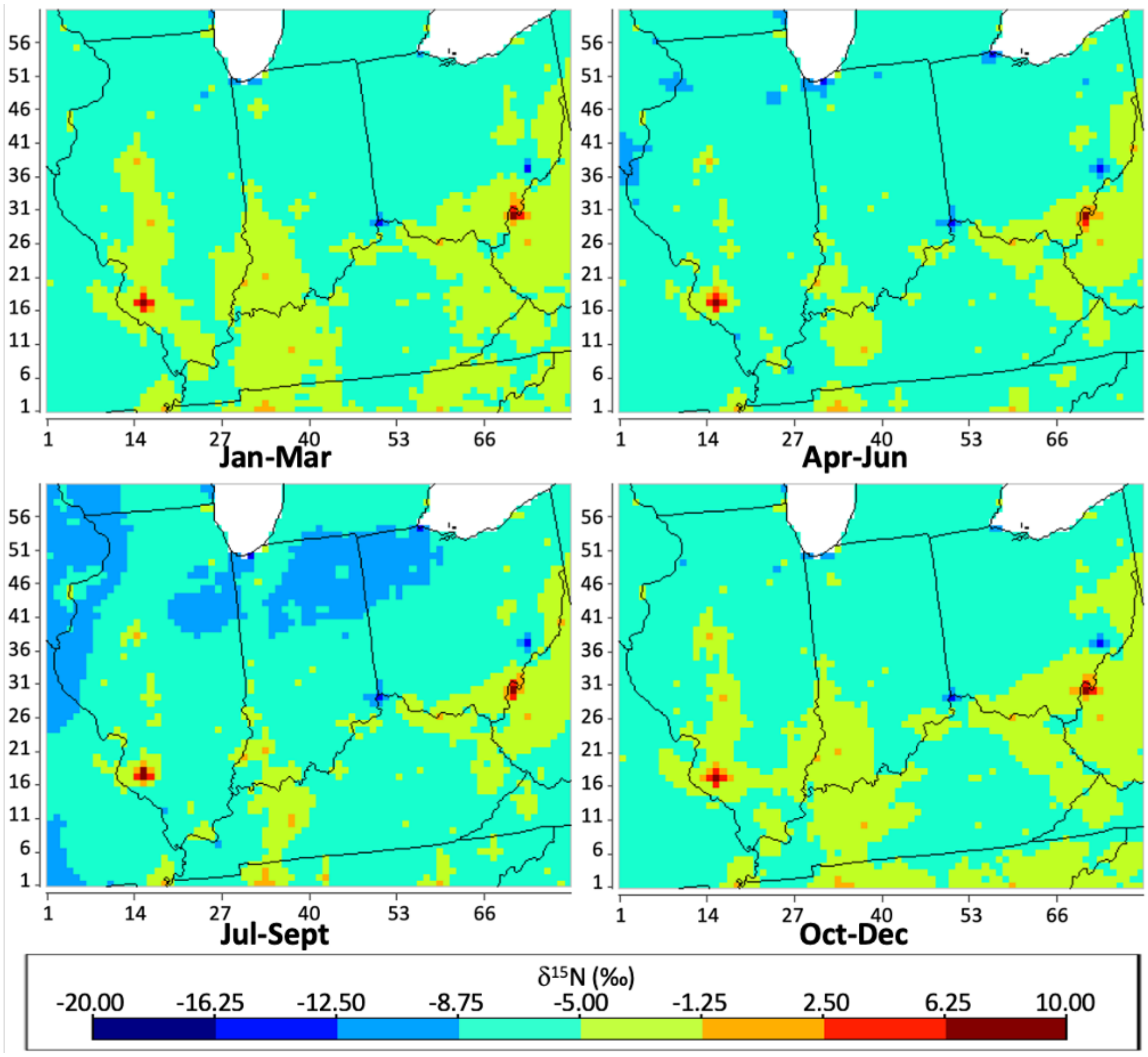

Figure S16: The extracted-domain simulation of the $\delta^{15}N$ value of atmospheric NO_x in each season (Winter: Jan-Mar; Spring: Apr-Jun; Summer: Jul-Sep; Fall: Oct-Dec) in per mil (‰) within IN, IL, OH, and KY, based on NEI-2002 and 2016 meteorology.

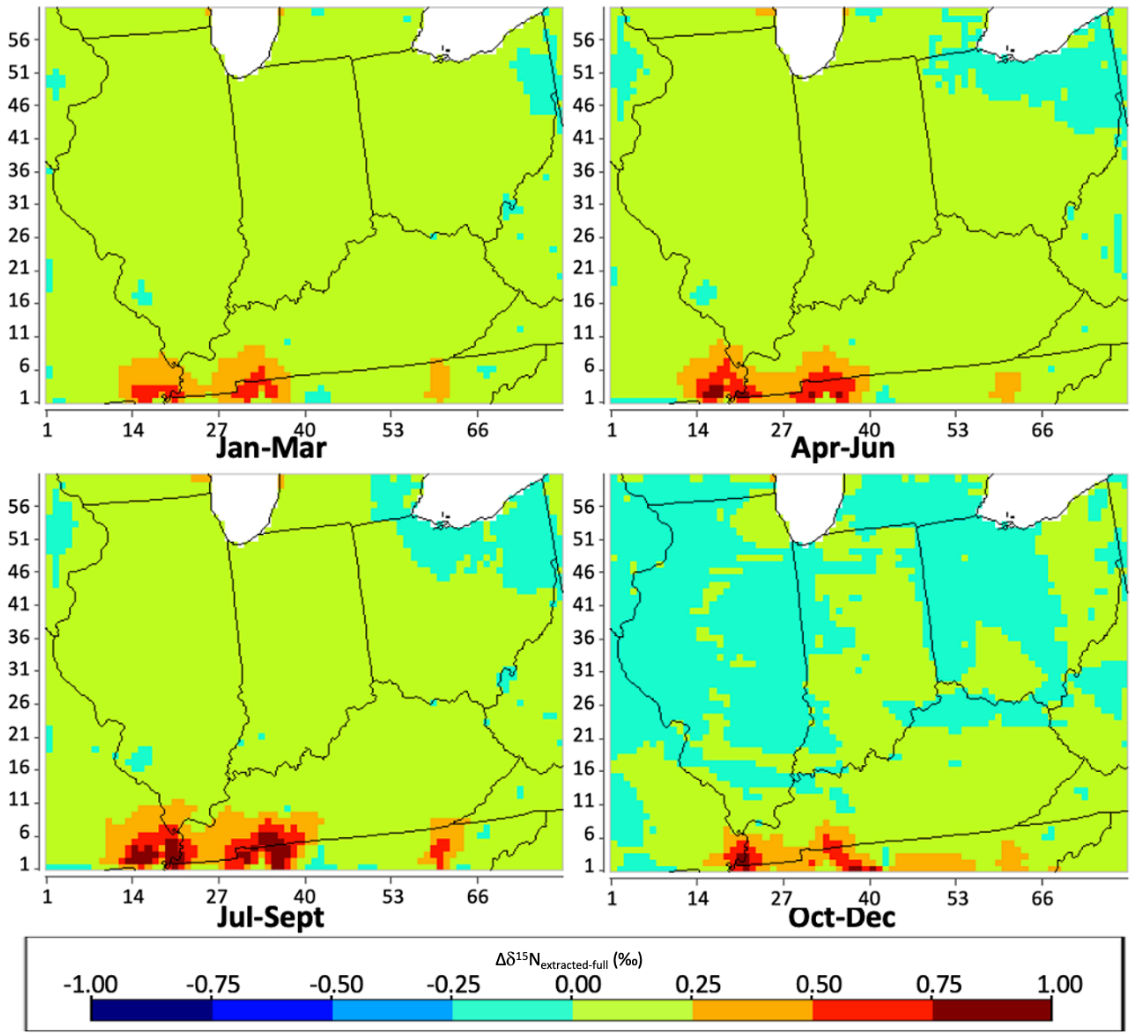

Figure S17: The geographical distribution of the difference between extracted-domain simulation and full-domain simulation of $\delta^{15}N$ value of atmospheric NO_x ($\Delta\delta^{15}N_{extracted\text{-}full}$) in each season (Winter: Jan-Mar; Spring: Apr-Jun; Summer: Jul-Sep; Fall: Oct-Dec) in per mil (‰) within IN, IL, OH, and KY, based on NEI-2002 and 2016 meteorology.

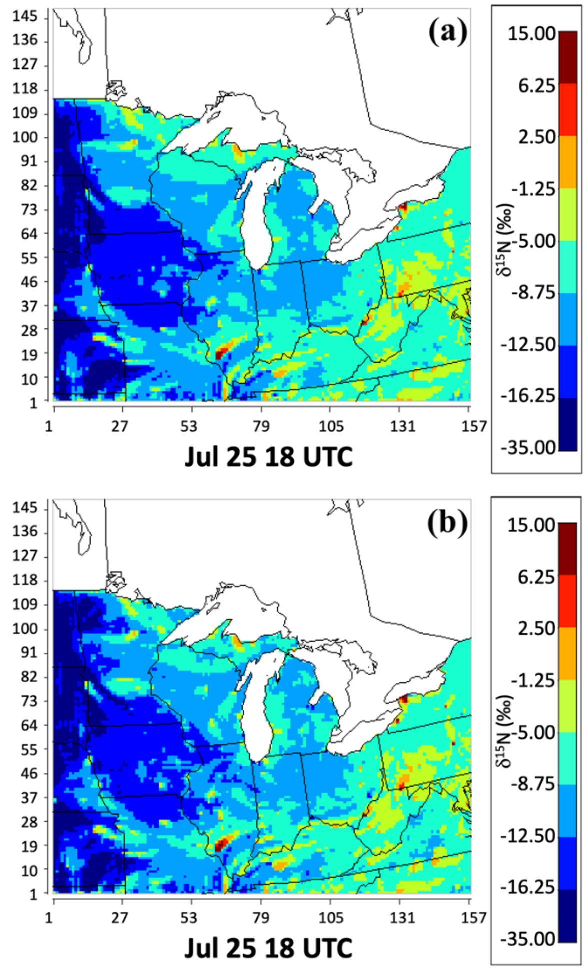

Figure S18: The $\delta^{15}N$ values of atmospheric NO_x under the "normal deposition" (a) and "enhanced NO_x loss" (b) scenario, based on NEI-2002 and 2016 meteorology.

Site ID	Site Name	County	State	Latitude	Longitude
IN20	Roush Lake	Huntington	IN	40.8401	-85.4639
IN22	Southwest Purdue Agriculture Center	Knox	IN	38.7408	-87.4855
IN34	Indiana Dunes National Lakeshore	Porter	IN	41.6318	-87.0881
IN41	Agronomy Center for Research and Extension	Tippecanoe	IN	40.4749	-86.9924
IL46	Alhambra	Madison	IL	38.8689	-89.6219
IL63	Dixon Springs Agricultural Center	Pope	IL	37.4356	-88.6719
OH09	Oxford	Butler	OH	39.5309	-84.7238
KY19	Cannons Lane	Jefferson	KY	38.2288	-85.6545

Table S6: NADP sites within the states of Indiana, Illinois, Ohio, and Kentucky

The only direct $\delta^{15}NO_x$ measurements within the domain occurred in West Lafayette, IN, located in northwestern Indiana and has an NADP (National Atmospheric Deposition Program) site near Purdue University. 30 NO_x samples were collected using denuder tubes between July 8 and August 5, 2016 (Fig. S18) from 8 am to 4 pm during the daytime, and from 9:30 pm to 5:30 am during the nighttime. The $\delta^{15}NO_x$ values were inferred from the measured $\delta^{15}NO_2$ and the calculated $\delta^{15}NO_2$ shift (Walters, Fang, & Michalski, 2018) and ranged from -23.3 to 0.2 ‰ during the daytime and ranged from -33.8 to -6.9 ‰ during the nighttime.

The SMOKE simulated $\delta^{15}N$ values of NO_x under the "emission only" scenario in West Lafayette show trivial monthly variations, and a small 1‰ seasonal trend (Fig. S19, right axis). The simulation shows that the $\delta^{15}N$ values stay around -4 ‰ from January to March, start to decrease in April until reaching -5 ‰ in June, and then start to increase in September until returning to -4 ‰ in November. These $\delta^{15}NO_x$ reflect that in West Lafayette mobile (on-road vehicle) is the dominant NO_x source (Fig. S19, left axis). The NO_x fraction from the mobile sector was between 0.8 and 0.9 throughout the year. Mobile NO_x during summer is 10 % lower than average, which could be explained by the decrease in vehicle traffic during the summer holiday, when most students return to their homes, and when biogenic and area sources slightly increase due to peak agriculture activity. This seasonal change in fractions results in the -1‰ over the summer period.

The $\delta^{15}N$ values of atmospheric NO_x under the "emission + transport" scenario, simulated by CMAQ, in West Lafayette show more obvious monthly variations and seasonal trends, comparing to the $\delta^{15}N$ values of NO_x emission (Fig. S20, in circles (○)). The simulation shows that the $\delta^{15}NO_x$ starts around -5‰ in January, which is about 1‰ lower than $\delta^{15}N$ of NO_x emission (Fig. S20, in squares (□)). During winter (Jan-Mar), the $\delta^{15}NO_x$ decrease slightly, and the difference relative to emission gradually increases. During spring (Apr-June), the more obvious decreasing trend of the $\delta^{15}N$ of atmospheric NO_x occurs, and the difference between the $\delta^{15}N$ of NO_x emission is larger than during winter. The $\delta^{15}N$ value reaches the minimum around -8‰ in July. During summer (Jul-Sept), the $\delta^{15}N$ of atmospheric NO_x starts to increase, and the difference between the $\delta^{15}N$ of NO_x emission decreases. During fall (Oct-Dec), the $\delta^{15}N$ of atmospheric NO_x increases, and the difference between the $\delta^{15}N$ of NO_x emission decreases, but with a slighter trend than during summer. The $\delta^{15}N$ of atmospheric NO_x ends at -5‰, 1‰ lower than $\delta^{15}N$ of NO_x emission. In addition to the change in the fractions of NO_x emission sources from April to September, which was just discussed above, the monthly variations and seasonal trend of the simulated atmospheric $\delta^{15}N(NO_x)$ are mainly driven by the strength of dispersion, mixing, and transport of the atmospheric NO_x emitted from different sources, indicated by the PBL height. The PBL height during the period from April to September is 90% higher than during the period from October to March, which is favorable for the mixture of isotopically lighter NO_x from the surrounding area (Fig. S20, in crosses (×)). Thus, the $\delta^{15}N$ of atmospheric NO_x diverges further from the $\delta^{15}N$ of NO_x emission.

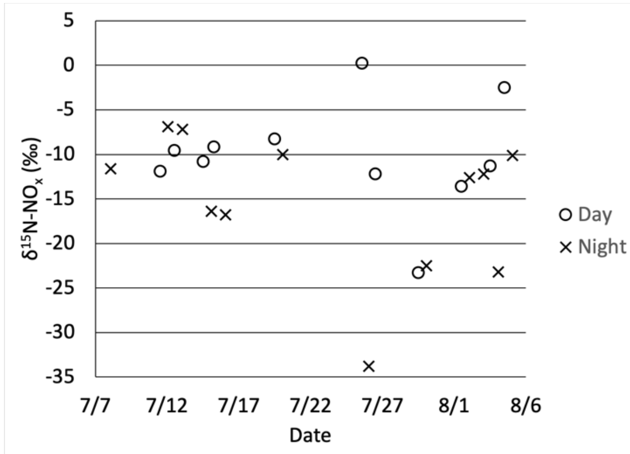

Figure S19: The $\delta^{15}N(NO_x)$ values measured at West Lafayette, IN between July 9 and August 5, 2016, from 8 am to 4 pm during the daytime (○), and from 9:30 pm to 5:30 am during the nighttime (×)

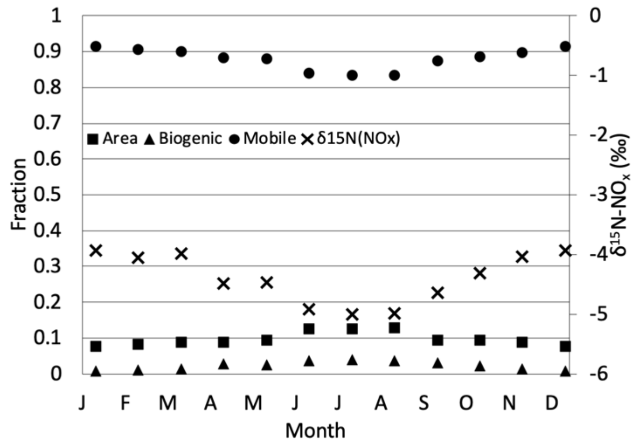

Figure S20: Fraction of monthly total NO_x emission by each SMOKE processing category (area [■], biogenic [▲], mobile [●]), and the monthly $\delta^{15}N$ values of total NO_x emission over the 12-km grid (right axis) over the 12-km grid that covers West Lafayette, IN simulated by SMOKE, based on NEI-2002.

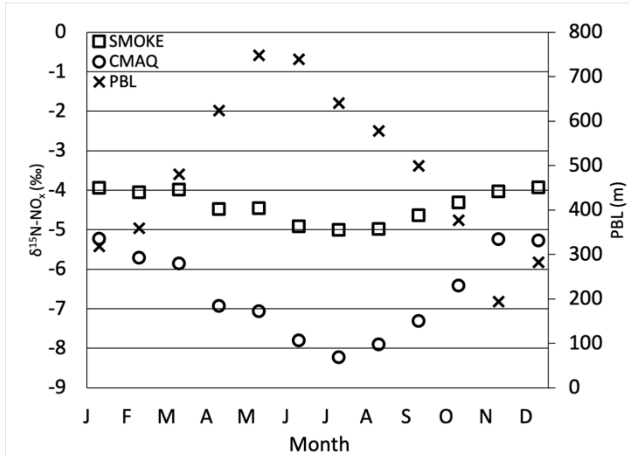

Figure S21: The monthly $\delta^{15}N$ values of total NO_x emission simulated by SMOKE (□) based on NEI-2002, the monthly $\delta^{15}N$ values of atmospheric NO_x simulated by CMAQ (○) based on NEI-2002 and 2016 meteorology, the monthly average of PBL height (×, right axis) over the 12-km grid that covers West Lafayette, IN.

	measurement	NEI 2002	NEI-2002 +WRF2016	NEI-2002 +WRF2002
min	-33.8	-12.2	-16.0	-15.6
max	0.2	-3.8	-3.7	-3.7
median	-11.2	-5.0	-7.9	-8.2
stdev	8.02	2.17	2.19	2.07

Table S7: Performance of $\delta^{15}N(NO_x)$ simulation for West Lafayette, IN

The model was used to predict $\delta^{15}NO_3^-$ and compared with the $\delta^{15}NO_3^-$ in deposition collected between 2001 and 2003 at several Midwestern NADP sites (Table S4). The $\delta^{15}N$ values of NO_x emission simulated by SMOKE at these sites show large monthly variations and a seasonal trend (Fig. S21a). The monthly boxes are the 1st and 3rd quantiles of the simulated monthly $\delta^{15}N$ of NO_x at the NADP sites. The whiskers represent the minimum and maximum values without outliers. There is a wide range of $\delta^{15}N(NO_x)$ values within each month, with a minimum during January (-11.2~ -3.9 ‰) and a maximum during September (-16.9~-4.6 ‰). The seasonal trend shows low $\delta^{15}N(NO_x)$ during summer, with the median around -10.3 ‰, and high $\delta^{15}N(NO_x)$ during winter, with the median around -9.4 ‰. The SPSS analysis result shows the monthly change of $\delta^{15}N$ values is dominantly affected by biogenic emission. The effect from point sources is minimal since most of the NADP sites are more than 12 km (grid size of SMOKE) away from the power plant. The NADP sites are not in big cities but close to soil emission. Thus, biogenic emission has the strongest effect on the $\delta^{15}N$ values of NO_x emission, accounting for 86.6% of the change on $\delta^{15}N(NO_x)$.

The $\delta^{15}N$ values of NO_x deposition simulated by CMAQ at these sites show similar monthly variations and seasonal trends as SMOKE (Fig. S21b). The ranges of $\delta^{15}N(NO_x)$ values within each month were narrower, comparing to the simulation from SMOKE, with a minimum during February (-8.7~ -4.4‰) and a maximum during August (-11.8~-4.2‰). The seasonal trend shows low $\delta^{15}N(NO_x)$ during summer, with the median around -7.4‰, and high $\delta^{15}N(NO_x)$ during winter, with the median around -6.0‰. Therefore, the CMAQ simulation inherits the monthly variations and seasonal trends from SMOKE, while the atmospheric NO_x becomes isotopically heavier, after taking atmospheric mixing and transport into account. As mentioned above, most of the NADP sites are located away from big cities and power plants. Thus, the atmospheric mixing and transport led to the isotopically heavier atmospheric NO_x.

The measurements of $\delta^{15}N$ values of NO_3^- at NADP sites from prior studies (Mase, 2010; Riha, 2013) show similar monthly variations and seasonal trend as both "emission only" and "emission + transport" simulations (Fig. S21). There is a wide range of $\delta^{15}N(NO_3^-)$ values within each month, with a minimum during January (10.4~17.2‰) and a maximum during August (1.0~16.7‰). The seasonal trend shows low $\delta^{15}N(NO_3^-)$ during spring, with the median around 9.3‰, and high $\delta^{15}N(NO_3^-)$ during winter, with the median around 13.0‰. The measured $\delta^{15}N$ values of NO_3^- have the same seasonal trend as the simulated $\delta^{15}N$ values of NO_x. Even considering the effect of atmospheric mixing and transport, the measured $\delta^{15}N$ values of NO_3^- are about 17‰ higher than the simulated $\delta^{15}N$ values of NO_x. The difference between CMAQ simulated and measured $\delta^{15}N$ values of deposition is caused by the following two factors: a). the mixture of isotopically lighter NO_x from the surrounding area discussed in section 3.3, and b). the net N isotope effect during the conversion of NO_x to NO_3^-, which will be addressed in future work.

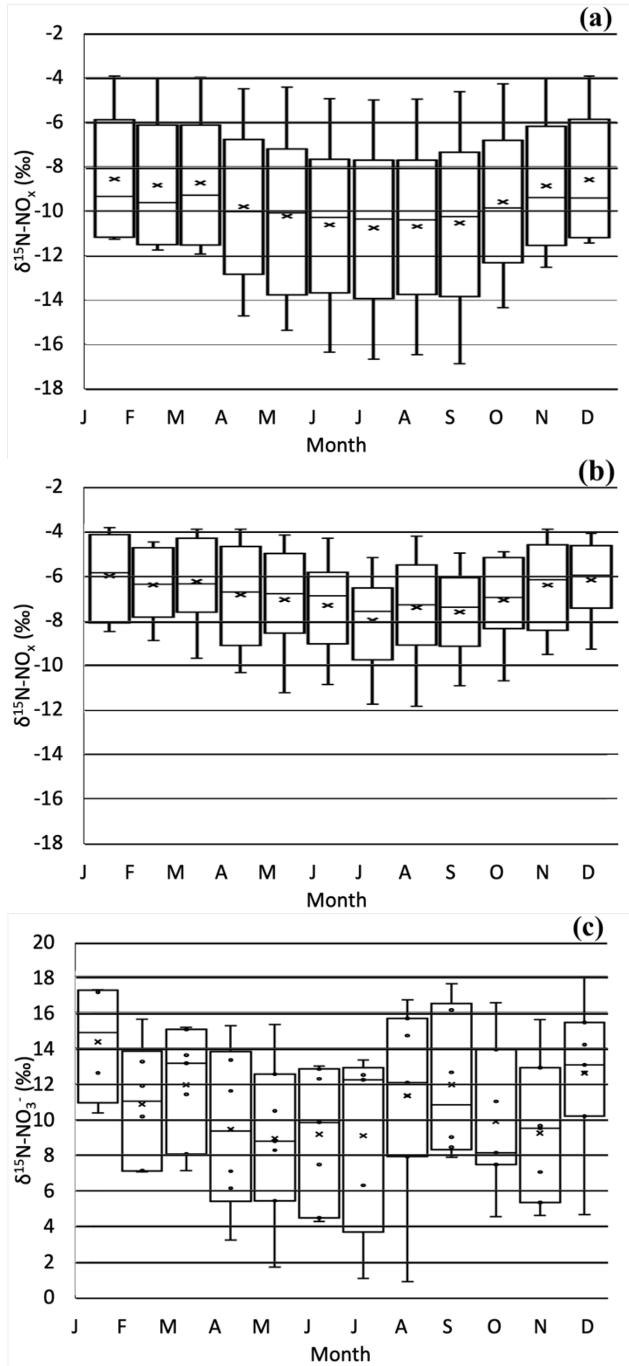

Figure S22: The emission only (a), emision + transport (b) CMAQ predicted $\delta^{15}N$ value of NO_x deposition at NADP sites within IN, IL, OH, and KY using NEI-2002 and 2002 meteorology, compared to the measured $\delta^{15}N$ of rain NO_3^- (c) from prior studies.

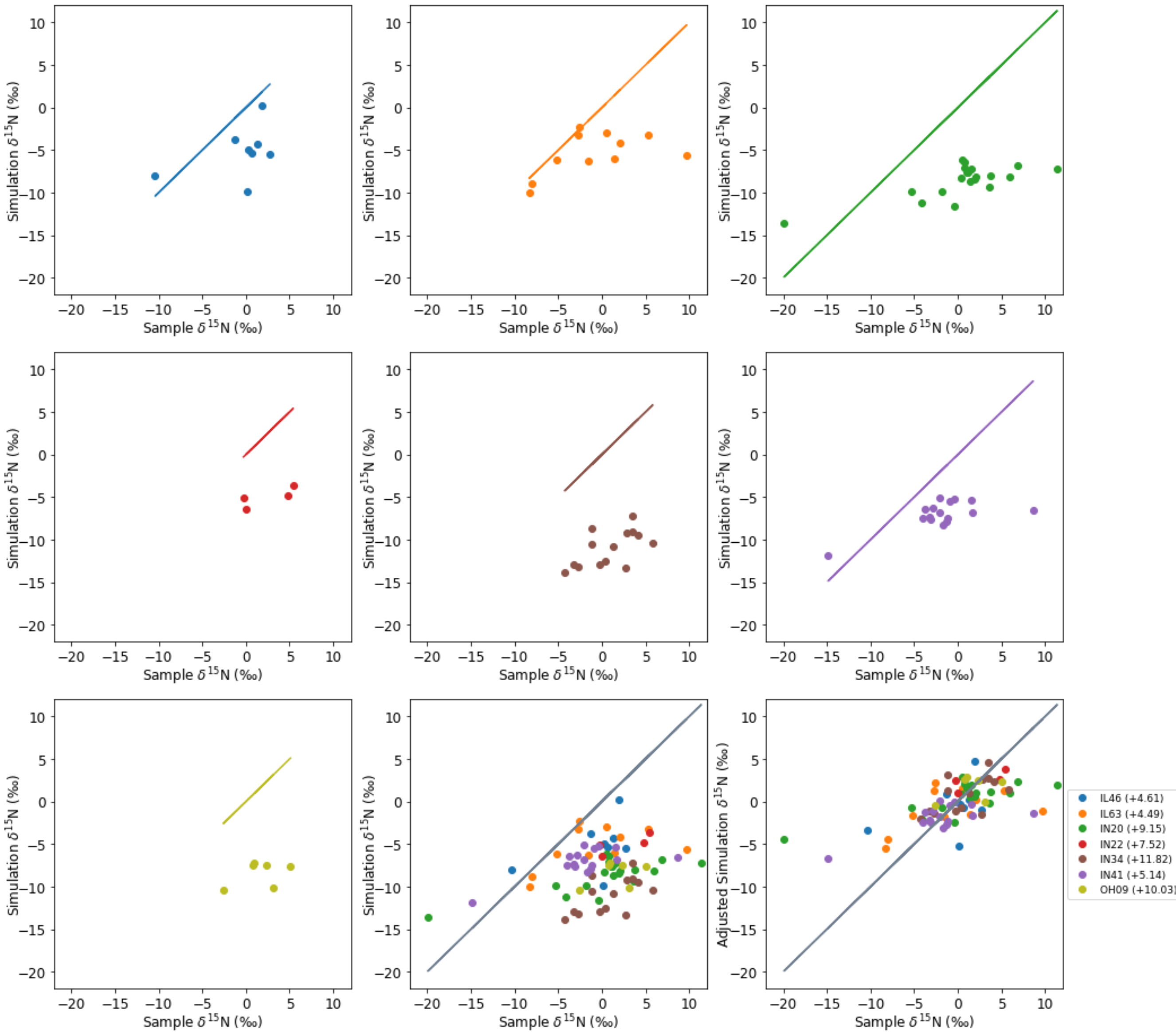

Figure S23: The emission + mixing + enhanced NO_x loss CMAQ predicted $\delta^{15}N$ value of NO_x deposition using NEI-2002 and 2002 meteorology compared to the measured $\delta^{15}N$ of rain NO_3^- at NADP sites within IN, IL, and OH.

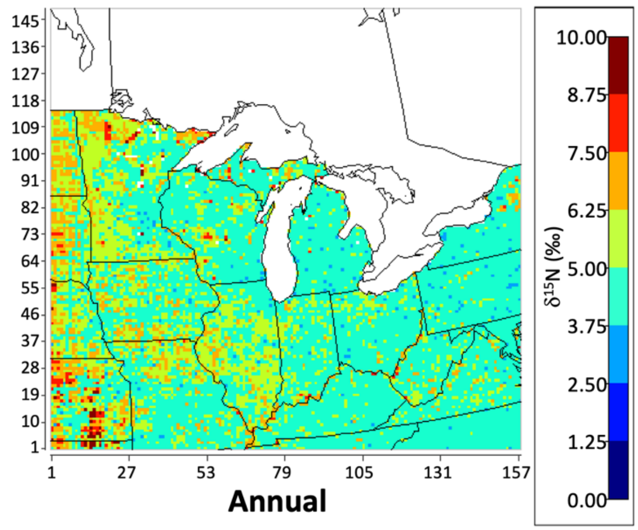

Figure S24: The uncertainties of $\delta^{15}N$ values in emission input dataset based on NEI-2002 are presented by color in each grid. The warmer the color, the higher uncertainties of $\delta^{15}N$ values.

References:

Grell, G. A., Dudhia, J., & Stauffer, D. R.: A description of the fifth-generation Penn State/NCAR mesoscale model (MM5), NCAR Technical Note NCAR/TN-398+ STR, 1994.

Houyoux, M.: Clean Air Interstate Rule Emissions Inventory Technical Support Document. US EPA, 2005.

Pierce, T. E.: Reconsideration of the Emission Factors assumed in BEIS3 for Three USGS Vegetation Categories: Shrubland, Coniferous Forest, and Deciduous Forest, 2001.

Pouliot, G., & Pierce, T. E.: Integration of the Model of Emissions of Gases and Aerosols from Nature (MEGAN) into the CMAQ Modeling System, in: 18th International Emission Inventory Conference, Baltimore, Maryland, 14 April 2009, 14-17, 2009.

Schwede, D., Pouliot, G. and Pierce, T.: Changes to the biogenic emissions inventory system version 3 (BEIS3), in 4th Annual CMAS User's Conference., 2005.

US Environmental Protection Agency: User's Guide to MOBILE6.1 and MOBILE6.2 Mobile Source Emission Factor Model, Tech. Rep. EPA420-R-03-010, 2003.

United States Environmental Protection Agency: Biogenic Emissions Landuse Database, Available from: https://www.epa.gov/air-emissions-modeling/biogenic-emissions-landuse-database-version-3-beld3, 2018.

Vukovich, J., & Pierce, T.: The implementation of BEIS3 within the SMOKE modeling framework, in: Proceedings of the 11th International Emissions Inventory Conference, Atlanta, Georgia, 15 April 2002, 15-18, 2002.